Additive manufacturing of functionalised atomic vapour cells for next-generation quantum technologies

IOP Publishing Quantum Sci. Technol. 10 (2025) 015019 https://doi.org/10.1088/2058-9565/ad8678

Quantum Science and Technology

OPEN ACCESS

RECEIVED
21 June 2024

REVISED
29 September 2024

ACCEPTED FOR PUBLICATION
14 October 2024

PUBLISHED
25 October 2024

PAPER

Additive manufacturing of functionalised atomic vapour cells for next-generation quantum technologies

Feiran Wang[1,3,*], **Nathan Cooper**[2,3], **Yinfeng He**[1], **Benjamin Hopton**[2], **David Johnson**[2], **Peng Zhao**[1], **Christopher J Tuck**[1], **Richard Hague**[1], **T Mark Fromhold**[2], **Ricky D Wildman**[1], **Lyudmila Turyanska**[1,*] and **Lucia Hackermüller**[2,*]

[1] Faculty of Engineering, University of Nottingham, University Park, Nottingham NG7 2RD, United Kingdom
[2] School of Physics and Astronomy, University of Nottingham, University Park, Nottingham NG7 2RD, United Kingdom
[3] These two authors contributed equally.
[*] Authors to whom any correspondence should be addressed.

E-mail: F.Wang@nottingham.ac.uk, Lyudmila.Turyanska@nottingham.ac.uk and Lucia.Hackermuller@nottingham.ac.uk

Keywords: additive manufacturing, quantum technologies, glass printing, vapour cell, atomic spectroscopy

Abstract

Atomic vapour cells are an indispensable tool for quantum technologies (QT), but potential improvements are limited by the capacities of conventional manufacturing techniques. Using an additive manufacturing (AM) technique—vat polymerisation by digital light processing—we demonstrate, for the first time, a 3D-printed glass vapour cell. The exploitation of AM capacities allows intricate internal architectures, overprinting of 2D optoelectronical materials to create integrated sensors and surface functionalisation, while also showing the ability to tailor the optical properties of the AM glass by *in-situ* growth of gold nanoparticles. The produced cells achieve ultra-high vacuum of 2×10^{-9} mbar and enable Doppler-free spectroscopy; we demonstrate laser frequency stabilisation as a QT application. These results highlight the transformative role that AM can play for QT in enabling compact, optimised and integrated multi-material components and devices.

1. Introduction

Growing understanding of fundamental quantum processes offers benefits in multiple sectors, from medicine [1, 2] and sensing applications [3–5], positioning and security [6, 7] to quantum computing [8]. However, realising these benefits requires innovations in quantum technology (QT) hardware, which must become smaller, lighter, cheaper, and better suited to the needs of specific applications. Additive manufacturing (AM) has the potential to transform QT [9, 10] by enabling miniaturised, robust devices that can be fabricated on demand with advanced architectures for enhanced operation, such as the innovative ultra-high vacuum (UHV)apparatus [11] previously reported. AM also presents opportunities for integration, both of novel hardware with existing equipment [12, 13] or of functionalised components within a larger device.

A critical QT component is the atomic vapour cell [14, 15], it underpins many technologies, spanning laser frequency stabilisation [16, 17], atom, molecule and ion-trapping [18–20] thermal vapour magnetometers [21], medical imaging [1, 2] and industrial scanning applications [22, 23]. However, vapour cells are difficult to manufacture, rely on the art of glass-blowing and are consequently limited in size and shape. The cells made by glass-blowing usually have simple geometrical forms, typically cylindrical or cuboidal, with dimensions on the order of centimetres and have limited scope for miniaturisation or customisation.

Planar lithographic processes [24, 25] and micro-electromechanical systems with anodic bonding [26–28] can produce microfabricated cells with great potential for miniaturisation, but lack 3D-versatility and offer only two optical interfaces, which is insufficient for some applications; nor do they have the same transformative potential for integration and customisation as AM.

AM can provide the means to overcome these limitations. AM of glass has been demonstrated using fused filament fabrication of molten glass [29, 30], selective laser melting with silica powder [31, 32] and

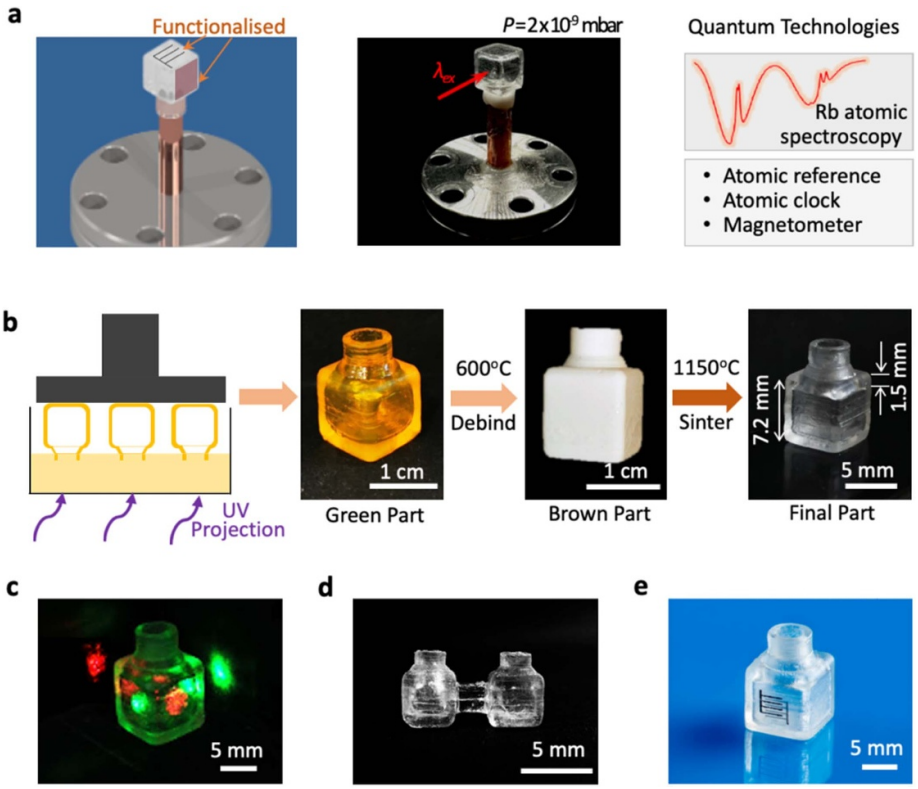

Figure 1. Additive manufacturing of a vapour cell for QT applications. (a) Schematic diagram of the AM vapour cell for QT applications. Left: illustration of the design of the cell mounted on an ultra-high vacuum flange via a copper tube. Middle: the photo of AM cell mounted for pumping to a pressure of 2×10^{-9} mbar and loading with Rb atomic vapour. Right: Doppler-free pump-probe absorption spectroscopy of Rb vapour in the AM vapour cell and applications of the AM vapour cell. (b) Vat polymerisation of glass vapour cells via DLP and optical images of the printed green, brown, and final parts following debinding and sintering steps. (c) Photographs of the printed cell with red and green laser beams propagating through the cell. (d) Photograph of two inter-connected cells. (e) Photograph of printed graphene and silver inter-digited electrodes on the AM cell for direct photon detection.

direct ink writing using silica sol-gel inks [33]. However, significant technological challenges such as limited resolution, evident surface roughness, cracking and low optical transparency have also been identified. Glass printing via the use of photocurable polymer/silica nanoparticle composites has led to optically useful constructs [34–39], but to date, the use of these formulations has been limited to structural ornaments, classical optics and fluidics.

Here we provide the first demonstration of an UHV compatible AM glass QT component and show that, by modifying the inks and printing procedures, transparent printed structures with integrated active elements (i.e. electronics, photodetectors) can be realised. These structures are of high optical quality, have the potential to transform vapour cell based QTs and open a route to the scalable manufacture of key components for spectroscopy and quantum sensing (figure 1(a)).

We describe the fabrication of glass vapour cells with sizes <1 cm^3 by a vat polymerisation method based upon digital light processing (DLP) of high loading silica nanoparticles resins (figure 1(b)). As a QT application, the cells are used to demonstrate atomic spectroscopy and show excellent vacuum performance, with pumped cells reaching pressures below 2×10^{-9} mbar and sustaining this pressure throughout the experiments. The cells were thermally tested up to 150 °C and were not noticeably degraded by exposure to high-temperature Rb vapour. We performed atomic vapour spectroscopy within the cells and demonstrated its application to laser frequency stabilisation [40] on the D2 line of ^{85}Rb.

The fabrication methodology is further applied to create complex cell geometries (figure 1(d)), while *in-situ* growth of metal nanoparticles is used to selectively tune the optical transmission of the produced glass, providing a clear demonstration of the versatility and transformative potential of such a method for creating optical materials for QT. These functionalised cells enable exciting applications, e.g. for the creation of sub-cm sized optically pumped magnetometers incorporating magnetic-field shielding conductors and photodetectors directly printed on the cell (figure 1(e)), thereby providing a significant jump in system flexibility and imaging resolution for non-invasive magnetoencephalography [41].

2. Results and discussion

2.1. AM of a vapour cell

To manufacture the glass vapour cell (figure 1(b)), a resin was formulated based on [34] containing fumed silica nanoparticles with an average size of 40 nm, dispersed in a mixture of 2-hydroxyethyl methacrylate (HEMA), tetra(ethylene glycol) diacrylate (TEGDA) and phenoxyethanol (POE). HEMA forms a solvation layer on the nanoparticles, hence allowing high silica loading of the resin. TEGDA is used to improve cross-linking, thus strengthening the mechanical structure of the printed part. A concentration of 50 wt% silica nanoparticles was achieved following a multi-step homogenising process [42]. The viscosity of the resin is 297 mPa · s at the shear rate of 1000 s^{-1}. For demonstration purposes, and to facilitate comparison with existing vapour cells used in commercial QTs, our cells have a cuboid shape featuring two pairs of parallel optical interfaces, in contrast to the single pair of parallel interfaces in wafer-based cells [43] and most glass-blown cells. The intended cell dimensions were 7.2 mm (L) × 7.2 mm (W) × 7.2 mm (H) with 1.5 mm wall thickness; the initial print was therefore 1 cm^3 with 2 mm thick walls, to allow for shrinkage. An inlet on one side (figure 1(b)) enables vapour loading and connection to our experimental apparatus.

To optimise the degree of curing during printing and obtain a high shape fidelity between the printed part and the design, the exposure time of each layer and the concentration of the absorber was adjusted by measuring the curing depth with different absorber concentrations (appendix A, figure A1). The optimal degree of polymerisation, curing depth and shape fidelity, was achieved with 6.5 s exposure time, 45 mW cm^{-2} power intensity and 0.035 wt% absorber content. A simulation of light-scattering from the silica nanoparticles showed an anisotropic distribution, however an isotropic degree of polymerisation can be achieved using this resin composition (appendix B, figure A2). The residual uncured resin was removed in washing and post-curing steps, resulting in a green part with good mechanical strength. Thermal debinding followed, with a gradual and uniform release of the internal mechanical stress, which was tailored to avoid cracking or collapse of the structure. The resulting debound porous brown part maintained the same geometry as the green part without volume shrinkage, but with a 51% weight loss due to the debinding process. To eliminate the porosity, the part was sintered in an inert argon atmosphere at temperature of T = 1150 °C for 12 h. This process allows the silica nanoparticles to merge and form amorphous glass. We note that the argon atmosphere prevented the risk of crystallisation, which was previously observed in synthesis of parts in the presence of oygen [44]. X-ray diffraction analysis confirmed the amorphos structure of the printed material (figure A3(a)) [45]. The density of the sintered part is 2.2 g cm^{-3} and the sintered part had no observable porosity (see scanning electron microscope images in figure A3(b)). The cells printed using this formulation showed high mechanical stability under external pressures and good optical flat-ness/transparency (see below) and enabled us to achieve and retain vacuum down to 2×10^{-9} mbar.

For our formulation, we observed about 27% shrinkage, both horizontally and vertically. The shrinkage of the part matched the estimation based on the solid weight concentration of the silica [42] and was accounted for in the design. The two pairs of parallel transparent flat surfaces of the cells allow two perpendicular beams to pass through with minimal distortion (figure 1(c)). An additional polishing step (Grit 1000 polishing paper) was introduced to reduce outer wall roughness.

2.2. Quantum sensing with additively manufactured cell

To demonstrate the suitability of the printed cells for QT applications, we performed rubidium spectroscopy in the cell. For this, the cell was mounted to an UHV flange via an annealed copper tube (figure 1(a)) and connected to a vacuum test system (figure 2(b)). The cells were leak tested and found to retain pressures down to 2×10^{-9} mbar, indicating that the printing methodology (resin formulation, printing and sintering) produces glass structures with no defects such as microcracking, porosity and incomplete polymer removal, making them suitable for UHV applications. The annealed copper tube allows for a separation of the cells from the vacuum apparatus after evacuation and use of the cell as a stand-alone device, via a standard copper pinch-off technique. The cell was then filled with a mixture of ^{85}Rb and ^{87}Rb via atomic dispensers. The geometry of the cell is also compatible with alternative filling methods, reported previously [46, 47]. The cell performance was first characterised through single-pass absorption spectroscopy. A single-mode, Gaussian laser beam with a diameter of 1.25 mm, a wavelength of 780 nm and a power of 0.06 mW was passed through the printed cell and detected on a photodiode (see figure 2(c)). The transmission through the cell without Rb vapour is >90%.

The frequency of the laser light was scanned across the D2 resonance of ^{85}Rb and fluorescence observed (figure 2(a)). The single-pass transmission spectrum (figure 2(d)) displays the typical Voigt-profiles with all expected features. The yellow line shows Doppler-free absorption spectroscopy for comparison—this was obtained with a standard, commercial 75 mm long glass cell. The Doppler-valleys corresponding to the D2 absorption lines of ^{85}Rb and ^{87}Rb are clearly resolved, showing single pass absorption along the ^{87}Rb $F = 2$

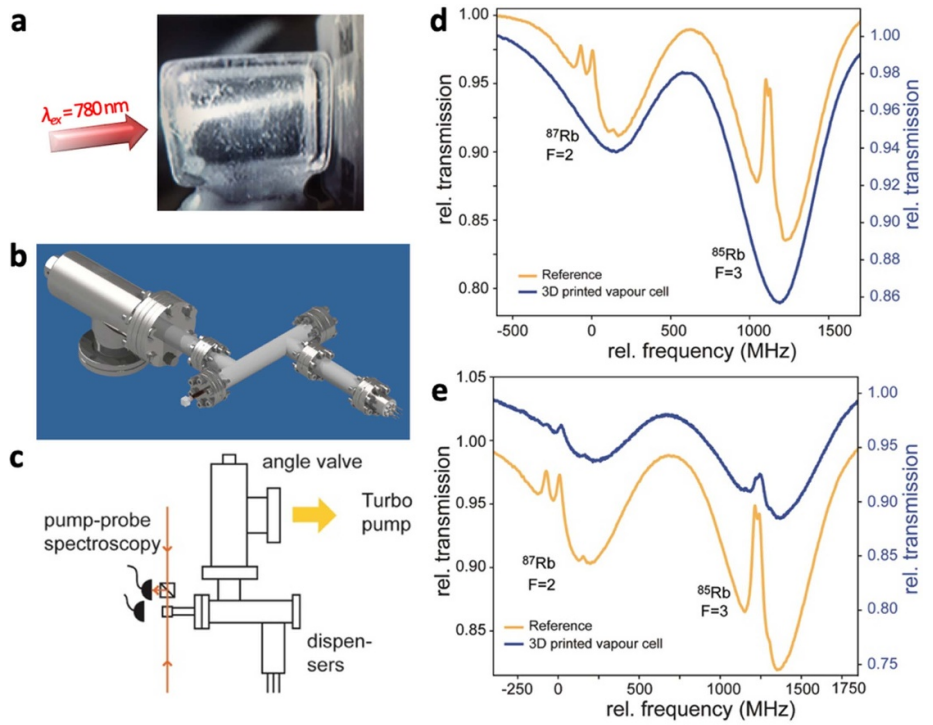

Figure 2. Absorption spectroscopy of Rb vapour in the AM vapour cell. (a) Rb fluorescence inside the cell under exposure to $\lambda_{ex} = 780$ nm laser light. (b) and (c) CAD model and a scheme of the vacuum and optical setups. (d) Single beam absorption spectroscopy. The scale of the reference signal (yellow) is vertically offset by 0.02 for clarity. (e) Doppler-free pump-probe absorption spectroscopy. For clarity, the scale of the reference signal (yellow) is vertically offset by −0.05. The frequency scale in (d) and (e) is set relative to the ^{87}Rb $F = 2 \rightarrow F' = 2 \times 3$ transition.

transition manifold and the ^{87}Rb $F = 3$ transition manifold (figure 2(d)). The frequency axis in figure 2(e) is given relative to the ^{87}Rb $F = 2 \rightarrow F' = 2 \times 3$ transition. As an example of QT-sensing, Doppler-free saturated absorption spectroscopy was demonstrated with the cell at room temperature. Counter-propagating linearly polarised beams with powers of 0.06 mW (probe) and 0.3 mW (pump) were set up as shown in figure 2(c). The transmission of the probe beam (blue line in figure 2(e)) shows the Doppler-free spectrum for the two transition manifolds ^{87}Rb $F = 2 \rightarrow F' = 1, 2, 3$ and ^{85}Rb $F = 3 \rightarrow F' = 2, 3, 4$. Though not all hyperfine states are fully resolved, the performance is comparable to a commercial cell, once the difference in optical path length is accounted for.

Doppler-free spectroscopy enables laser frequency stabilisation ('locking') to the hyperfine transitions. We stabilised a laser to the ^{85}Rb $F = 3 \rightarrow F' = 3 \times 4$ crossover transition and thus demonstrated that the cell can be used as a frequency standard. The laser current was modulated with a frequency of 100 kHz, the photodiode signal was demodulated and an error signal obtained that corresponds to the derivative of the spectroscopy signal. This signal was used to frequency-stabilise the laser through feedback to the laser diode drive current.

To analyse the resulting frequency stability, the error signal was recorded over a period of twenty minutes, while the laser was frequency locked via the signal from the printed vapour cell. By analysing the error signal, the Allan deviation was obtained for the locked laser and compared to the unlocked or free-running laser (see figure 3). The stabilisation based on the printed vapour cell reaches $\Delta F/F = 2 \times 10^{-10}$ at long interrogation times ($t \sim 1$ s), an improvement of 1–2 orders of magnitude in comparison with the free-running laser, and provides significant stability improvements on all time scales. This demonstrates that the printed vapour cell can provide stable, Doppler-free laser locking. A similar setup based on polarisation can be used to operate the cell as a magnetometer [43, 47]. We compared the locking performance to a standard 75 mm long commercial vapour cell (Thorlabs, made by conventional glass blowing). The printed cell shows comparable performance to the commercial cell with the benefit of 5 access sites and miniaturised shape. The primary difference between the printed cell and commercial cells comes from the difference in optical path length and is not related to its manufacture or composition. Taking the 15 times difference in optical path length into account, the Allan deviation normalised to optical path length is similar or slightly better for the printed cell (figure A5).

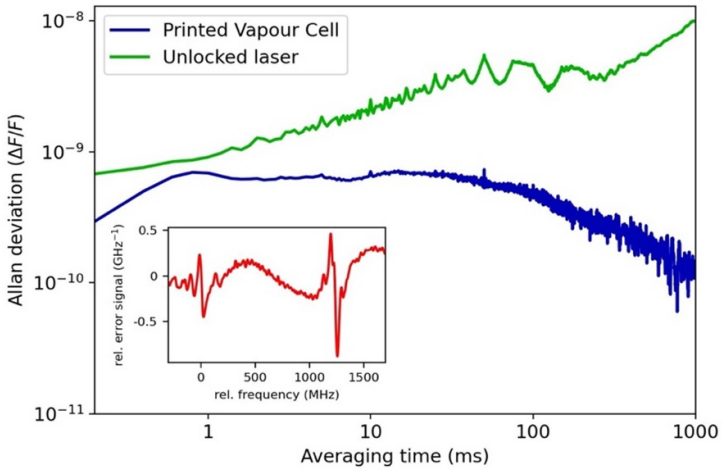

Figure 3. Allan deviation of the unlocked laser, and with the laser locked using the printed vapour cell. Inset: the error signal (red) is shown for reference.

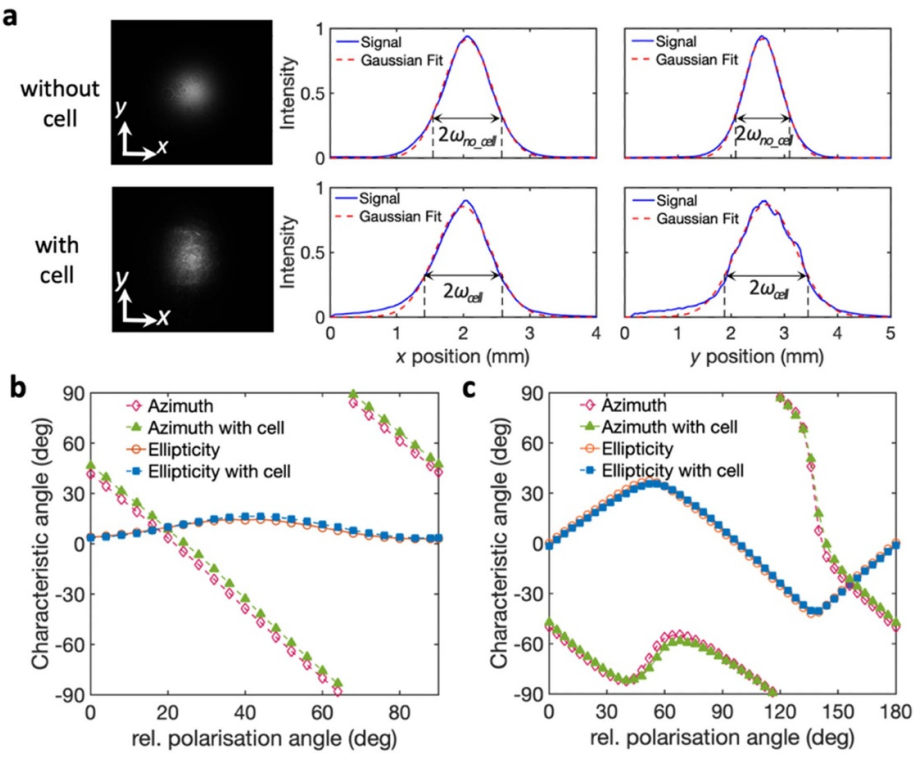

Figure 4. Transmission and polarisation measurement of the AM vapour cell. (a) Beam profile of a 780 nm test laser beam with and without passing through the cell. (b) Azimuth and ellipticity measured using a polarisation analyser for varying angles of polarisation, with and without the presence of the printed vapour cell, for initially linearly polarised light. (c) The Azimuth and ellipticity for varying angles of a preceding quarter-waveplate, with and without the presence of the printed vapour cell, for initially linearly polarised light.

To evaluate the applicability of printed vapour cells for magnetometry and polarisation dependent QT applications, the effect of the printed cell on beam shape and the polarisation of laser light (780 nm) was investigated with an internal vacuum of 2×10^{-9} mbar. By analysing the Gaussian beam profile with and without the cell in the optical path, negligible distortion and a slight increase of the beam waist from the horizontally printed faces is observed [$\omega_{\text{no\_cell}} = (0.51 \pm 0.1)$ mm and $\omega_{\text{cell}} = (0.56 \pm 0.1)$ mm], as shown in figure 4(a). For the vertically printed faces, the beam waist increased by ∼50% [$\omega_{\text{no\_cell}} = (0.51 \pm 0.1)$ mm and $\omega_{\text{cell}} = (0.78 \pm 0.1)$ mm] most likely due to curvature of the internal surface, which can be considered in future designs. Small undulations are caused by the layer-by-layer printing process.

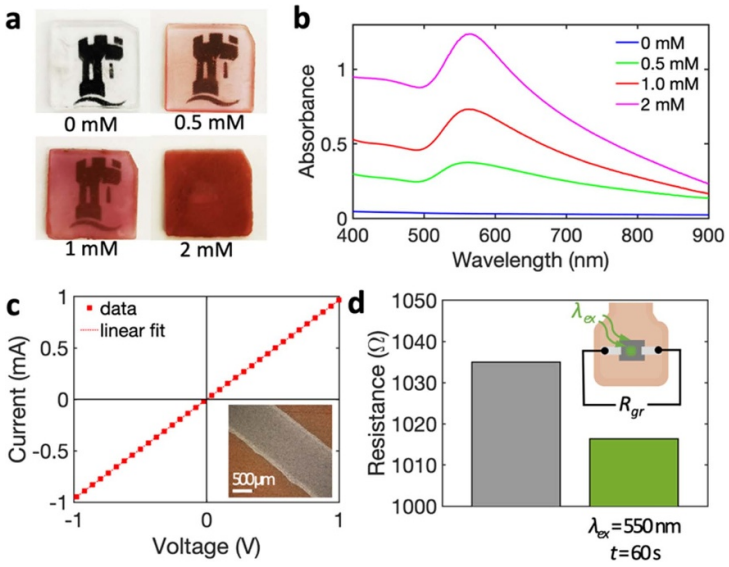

Figure 5. Functionalisation of AM glass—AuNP doping and graphene tracks. (a) Photographs of printed glass slabs of 1.25 × 1.25 cm, with different concentrations of AuNP dopant, positioned over the University of Nottingham logo. (b) Measured absorbance of glass printed with different concentrations of AuNP dopant. (c) Representative *I(V)* dependence of a graphene track (10 mm by 2 mm) inkjet printed onto the 0.5 mM AuNP doped glass and (inset) optical microscopy image of the printed graphene track. (d) Electrical resistance, R_{gr}, of the graphene track printed onto an AuNP doped glass slab (0.5 mM) measured in the dark and under continuous illumination with green laser light ($\lambda = 550$ nm, $P = 25$ mW). Inset: Schematic of the measurement scheme.

The effect of the printed vapour cell on polarisation was analysed, for linearly polarised light, for various input polarisation angles obtained via tuning of a half-wave plate, with a measurement of the azimuth and ellipticity taken every 4° using a polarisation analyser. The measurements with and without the printed vapour cell (figure 4(b)) revealed negligible change (comparable to the resolution of the instrument) of azimuth and ellipticity when the cell is present in the optical path. The half-wave plate was then switched for a quarter-wave plate and the same measurement technique was repeated, to study the effect of the cell on elliptically polarised light. The results are shown in figure 4(c).

2.3. Functionalisation of AM vapour cell

Our method of 3D-printing vapour cells offers exceptional opportunities for improved QT. We are able to demonstrate a range of desirable features for vapour cell performance that are only made possible through AM. The geometric design freedom of AM enabled printing of two inter-connected cells with a variable length tube (two 4.5 mm cuboid cells connected with a 3 mm channel, figure 1(d)), thus offering increased optical depth, while by overprinting the cell with conductive materials (figure 1(e)) we demonstrate integration and compactification potential for sensors and detectors.

Tuneable modification of the optical transparency of glass has previously been achieved by dipping the brown part into solutions containing metal salts [34, 48, 49]. We propose a facile method where AuNP are formed *in situ* to modify the glass absorption in the visible wavelength range. Gold salt, $AuCl_3$, was added to the resin before printing to form Au nanoparticles (AuNPs) *in situ* by photothermal reduction process, thereby causing the glass to acquire a cranberry-red colour [50]. An absorption peak, characteristic of AuNPs, was observed at a wavelength of ∼565 nm (figure 5(a)) for the glass produced with 1 mM of $AuCl_3$, indicating the formation of AuNPs with size of about 20 nm. By varying the $AuCl_3$ concentration from 0 to 2 mM, the colour of the resulting glass changed to dark deep red (figure 5(a)), indicating the formation of larger size AuNPs. The absorption peak shifts to a longer wavelength from 562 nm for 0.5 mM to 567 nm for 2 mM and its intensity increases (figure 5(b)). The increase of the nanoparticle size and their density is expected with increasing concentration of precursor salt [51, 52]. Importantly, the doped glass retains sufficient optical transparency in the near infrared range, as required for Rb atomic spectroscopy, while filtering out shorter wavelength visible light from environmental sources. In the context of magnetometer cells, doped glass also offers the exciting exploitation of surface plasmon resonances (SPRs) of AuNP for local optically-activated heating, which can be used to achieve higher vapour pressure in the cell faster than standard current-based heating methods [53].

To demonstrate SPR, we inkjet printed a graphene (iGr) track [10 mm (L) × 2 mm (W)] onto one side of the glass slab as shown in figure 5(c). Upon exposure of the undecorated side of the AuNP-glass to green laser

light (550 nm), the resistance of the graphene track decreased by about 2% from 1035 Ω to 1016 Ω after 60 s exposure (figures 5(d) and A4). This is a typical change in resistance expected for a temperature increase of 30 °C. An equivalent track on undoped glass produced no detectable response under the same conditions (figure A4(a)), confirming that the localised heating was generated by SPR of AuNPs. For medical sensing application, e.g. magnetometers for brain imaging, this is a very relevant feature as the vapour pressure can be increased without heating coils and without raising the temperature of the environment; this reduces power dissipation and the need for thermal insulation, hence allowing the sensor to be brought closer to the tissues being studied. The technique also enables glass with a customisable optical absorption range within one glass structure(see figure A4(b)).

Similarly to the overprinted graphene path, the vapour cell can be surface-decorated with other functional materials, including conductive layers/devices that can be inkjet printed onto the cell. Using the inkjet-printing method described in [54], a pair of 300 μm wide interdigitated conductive tracks was deposited using silver nanoparticle ink and graphene inks (figure 1(e)), with a sheet resistance of 0.53 Ω sq^{-1} and 207 Ω sq^{-1} respectively, which is comparable to the values achieved on other substrates [54, 55]. The conductive tracks exhibit good adhesion to the printed glass cell, enabling e.g. heating or magnetic field shielding elements that are co-manufactured with, and integral to, the vapour cell. The AM build process also facilitates integration of other active components, such as inkjet-printed perovskite photon sensors [56], which can be used for *in situ* monitoring. Integrating control components within the cell enables some interactions not possible with external components, such as the plasmonic heating described above or magnetic field control with high spatial resolution. Additionally, it reduces the size and power requirements of conventional control hardware, potentially allowing application of known interactions within novel applications; for example, it may allow sensors based on such cells to be brought closer to biological subjects, or improve the performance of atomic sensor arrays by reducing cross-talk between modulation coils.

3. Conclusions

AM of transparent glass elements has immense potential to improve components for QT. A glass vapour cell has been produced by DLP and a wide range of functionalising capabilities have been demonstrated, including integrated 3D printed electronics and active optoelectronic components for enhanced device functionality, and wavelength-selective absorption for surface plasmonic heating.

The printed vapour cell was successfully pumped to the UHV regime (2×10^{-9} mbar) and loaded with atomic rubidium vapour. The cell exhibits high transparency and polarisation stability, enabling the observation of atomic spectroscopy, including signature Doppler-valley and sub-Doppler features. Used as a frequency reference, laser stabilisation has been achieved with an Allan deviation $\Delta F/F < 10^{-9}$, limited by electronic feedback hardware, not the AM vapour cell.

This work will inspire new AM-QT research directions, for example, how the sensitivity of a spin-exchange relaxation-free magnetometer based on modified surfaces in a 3D printed vapour cell compares to established designs [26]. The process could enable manufacture of >40 glass cells (green parts) per lab-based printer per hour and the times required for debinding and sintering each cell could be effectively shortened with large volume furnaces.

Our methods opens the way for the creation of novel, high-performance sensors based on functionalised glass vapour cells for enhanced QT devices, such as magneto-encephalography sensors, atomic clocks, inertial sensing accelerometres and gyroscopes, atom/ion trapping quantum computers and more. The upscalability of the AM process, together with good optical quality and high vacuum performance, makes such devices a scalable, convenient and customisable fabrication solution for many QT application sectors.

Experimental methods

Resin formulation

A mixture of 60 vol% HEMA, 10 vol% TEGDA and 30 vol% POE was prepared, and blended with 0.2 wt% of bis (2,4,6 trimethylbenzoyl) phenylphosphineoxide as a photoinitiator, 0.1 wt% of hydroquinone monomethyl ether as an inhibitor and 0.035 wt% of Sudan Orange UV absorber. Aerosil OX50 silica nanopowder (50 wt%) was added in 10 small doses with 15 min bath sonication to prevent agglomeration. The final slurry was further bath sonicated for 30 mins and then degassed at a low pressure of 200 mbar for 3 min.

AM process

The design was printed on a Cellink Lumen X printer (45 mW cm^{-2} UV power intensity at 405 nm) with 50 μm hatching distance and 6.5 s exposure time for each layer. The printed part was immersed in propylene glycol methyl ether acetate and washed using a tube roller at 80 rpm for 5 min to remove the residual non-polymerised material. The washing cycle was repeated three times. Then the part was exposed to ultraviolet floodlight using a Wicked Curebox for 10 min for post-curing.

Post-process debinding and sintering

The green part was debound in a high-temperature furnace (Carbolite HRF 7/22 box furnace) with the ambient temperature being increased at 0.35 °C min^{-1} to $T = 130$ °C, held at this temperature for 2 h, then increased at the same rate to 320 °C for 4 h and 600 °C for 2 h. The resulting brown part was further sintered at $T = 1150$ °C for 12 h with 3 °C min^{-1} heating and cooling rates under 1 bar argon flow using a tube furnace (Carbolite STF 15/50).

Functionalisation

Doping with Au nanoparticles was achieved by adding $AuCl_3$ to the resin, with final concentrations of 0.5 mM, 1 mM and 2 mM, before adding fumed silica powder. Conductive tracks were deposited with a 300 μm wide interdigitated design using a Dimatix DMP-2831 inkjet printer and a Samba cartridge of 2.4 pl drop volume. Three layers of AgNP ink (XTPL IJ36) were deposited using a 20 μm drop spacing and ten layers of graphene ink (Merck 793663) were printed using 10 μm drop spacings.

Electrical and optical characterisation

The sheet resistance of the printed silver and graphene samples was measured using a Keithley 2400 sourcemeter and a micromanipulator with a four-probe method, also known as the Kelvin technique, to eliminate contact resistance. Each *I–V* curve was measured three times using both forward and backwards scanning. The derivative of the *I–V* curve reveals the conductivity of the printed line with the exact geometry measured by an optical microscope.

Characterisation of polarised light

The laser beam was set up to pass through a linear polariser and a waveplate (either quarter-wave or half-wave as appropriate), before passing through the printed vapour cell, which was under internal vacuum so that no gases in the cell could alter the polarisation.

Atomic spectroscopy

The cell was connected to a UHV-flange via an annealed copper tube and attached to the tube using UV-curing glue (Dymax OP-67-LS). The system shown in figure 2(b) was used to demonstrate the vacuum compatibility of the cells. Following bake-out for 24 h at 150 °C and leak-testing, pressures down to 2×10^{-9} mbar were achieved. Laser light resonant with the rubidium absorption lines from a Toptica 110 tapered amplifier laser was then guided into the cell and the resulting absorption measured on a Thorlabs DET10A amplified photodiode. Doppler-free spectroscopy was obtained using a pump-probe setup as shown in figure 2(b) with 0.06 mW probe beam power and 0.3 mW pump beam power in beams with a diameter of 1.25 mm. The cell was used under UHV conditions for atomic spectroscopy over a period of 6 months, with no degradation of performance detected in this time. The commercial reference vapour cell of Ø25.4 mm × 71.8 mm was purchased from Thorlabs (GC25075-RB). For laser locking with this commercial cell, the probe beam is retro-reflected back through the cell, instead of separate probe and pump beams.

Data availability statement

All data that support the findings of this study are included within the article (and any supplementary files). The authors are happy to provide additional information upon request.

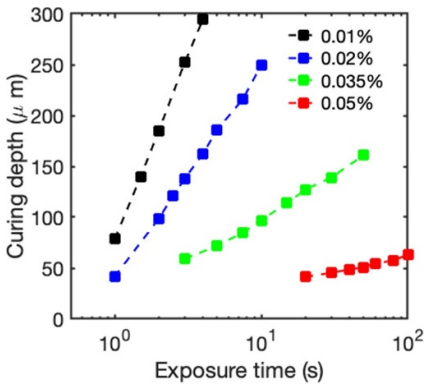

Figure A1. Measured curing depth versus exposure time under irradiation of 45 mW cm^{-2} UV light for resins with concentrations of UV absorbers of 0.01%, 0.02%, 0.035% and 0.05%.

Acknowledgment

This work was supported by the Engineering and Physical Sciences Research Council, EPSRC [grant numbers EP/P031684/1, EP/T001046/1, EP/M013294/1]. The QT experiment was also supported by the grant 62420 from the John Templeton Foundation; the Innovate UK [project number 133086]; the EPSRC [grant numbers EP/R024111/1, EP/Y005139/1, EP/Z533166/1]; and the European Comission grant ErBeStA (no.800942). We acknowledge University of Nottingham, Wolfson facilities and Miss Rebecca Saint for assistance with the XRD studies.

Appendix A. Optimisation of printing parametres for the resin

By comparing the curing depth of the resins containing different concentrations of UV absorbers of 0.01 wt%, 0.02 wt%, 0.035 wt% and 0.05%, as shown in figure A1, the 0.035 wt% was chosen as the optimum for the 50 μm layer thickness used by the Lumen X printer which results in a high geometry fidelity at short printing times.

Appendix B. Modelling of scattered light of nanoparticles in the resin

Previous studies have highlighted that the existence of nanoparticles in UV curable resins promotes the curing in depth due to the light scattered from the nanoparticles [57], and the extra energy overcures the photocurable material in the curing layer which reduces the printing resolution or even interferes with the curing of the next layer in DLP printing (figure A2(a)). Following previous work on the modelling of polymerisation kinetics [58], the degree of curing caused by scattering in our resin formulation was calculated and confirmed that the formulated resin successfully suppressed the curing inhomogeneity caused by scattered light around the nanoparticles. The scattered light intensity due to Rayleigh scattering of one OX 50 nanoparticle can be calculated by

$$I = I_0 \frac{1+\cos\theta}{2R^2}\left(\frac{2\pi}{\lambda}\right)^4\left(\frac{n^2-1}{n^2+2}\right)^2\left(\frac{d}{2}\right)^6 \tag{A1}$$

where $I_0 = 45$ mW cm^{-2} is the intensity of the Lumen X printer used in this work, R is the distance from the particle, θ is the scattering angle, $n = 1.45$ is the refractive index of the resin, $d = 40$ nm is the diameter of the nanoparticle and $\lambda = 405$ nm is the wavelength of the light. Taking $R = 1.02\,d$ which is the mean distance between two particles that matches the 50 wt% of nanoparticles in the resin, the distribution of scattered light intensity is anistropic and the scattered light is 1.9 times stronger along the incoming UV light (z direction) than the perpendicular x–y plane (figure A2(b)).

Despite the anistropic angular distribution of scattered light intensity, the formulated resin exhibit a isotropic degree of polymersaiton and this can be verified by the following kinetcs modelling of the polymerisation process. During photopolymerisation, free radicals are genetrated and recated with vinyl groups to form a chain of large free radical molecules, which can then terminate into stable polymer chains. The consumption of the vinyl groups during polymerisation, χ, can be described using kinetic relation which combines two submodels [59], the classical theory of free radical polymerisation with the

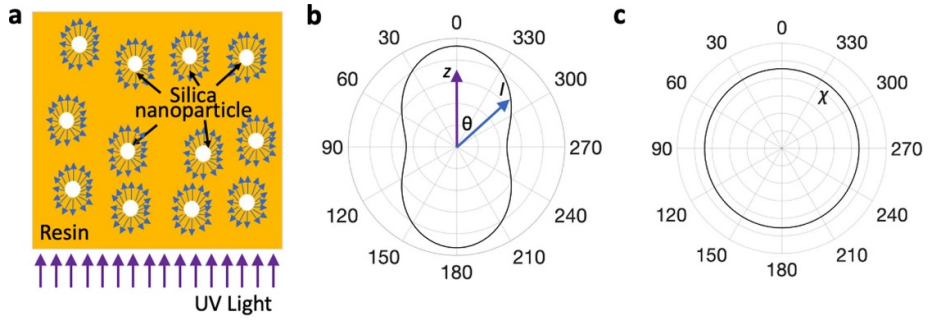

Figure A2. (a) Sketch showing the light scattering by the silica nanoparticles in the resin. (b) Light scattering power density distribution from a silica nanoparticle when $R = 1.02\ d$ from equation (A1). (c) The resulting, homogeneous consumption of the vinyl group χ due to scattering around the nanoparticle from equation (A2), when $R = 1.02\ d$ is chosen.

consumption χ_p, and an autoacceleration effect with the consumption χ_a. Using the method described in [58], the degree of polymerisation during the UV exposure can be predicted based on the light intensity and the composition of the formulated resin. The total consumption of the vinyl groups can be obtained by

$$\chi = \chi_p + \chi_a = \chi_{max,p}\left(1 - e^{k_p \Lambda}\right) + \frac{\chi_{max,a}}{1 + e^{k_a(\Lambda - \Lambda_C)}} \tag{A2}$$

where $\Lambda = \sqrt{I}t$ is the UV radiation dose ($t = 6.5$ s is the exposure time), $\chi_{max,p} = 0.2079$ and $\chi_{max,a} = 0.5729$ are the maximum degrees of vinyl group consumption that can be achieved by the classical radical polymerisation and the autoacceleration polymerisation rescpetively. The rate constant of free radical polymerisation $k_p = -0.0083\ (\mathrm{kg/s})^{-1/2}$, the rate constant for the autoacceleration stage $k_a = -0.1258\ (\mathrm{kg/s})^{-1/2}$ and the required UV radiation dose to achieve half of the maximum degree of vinyl group consumption at the autoacceleration stage $\Lambda_C = 14.0719\ (\mathrm{kg/s})^{1/2}$ are parameters determined by the compositions of monomers, photoinitiators and absorbers in the formulation utilising the method described in [58], the angular distribution for degree of curing from the modelling in figure A2(c) has an isotropic distribution along all directions, which indicates a similar degree of curing along all directions.

Appendix C. Characterisation of printed and functionalised glass structures

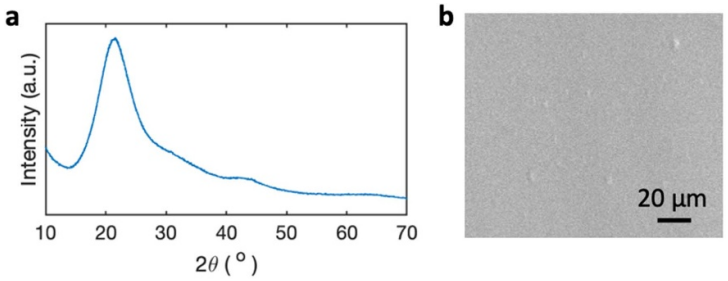

Figure A3. (a) x-ray diffraction (XRD) pattern and (b) a representative cross-section scanning electron microscope (SEM) image of the final printed glass part showing amouphous strucuture after sintering.

Appendix D. Laser locking comparison to Thorlabs 75 mm vapour cell

For laser frequency stabilization, we compared the performance of our printed vapour cell to a standard Thorlabs 75 mm vapour cell. For laser locking with this cell, the probe beam is retro-reflected back through the cell, instead of separate probe and pump beams. Note that the total path length is 15 times that for the printed vapour cell. The resulting Allen deviation is shown in figure A5.

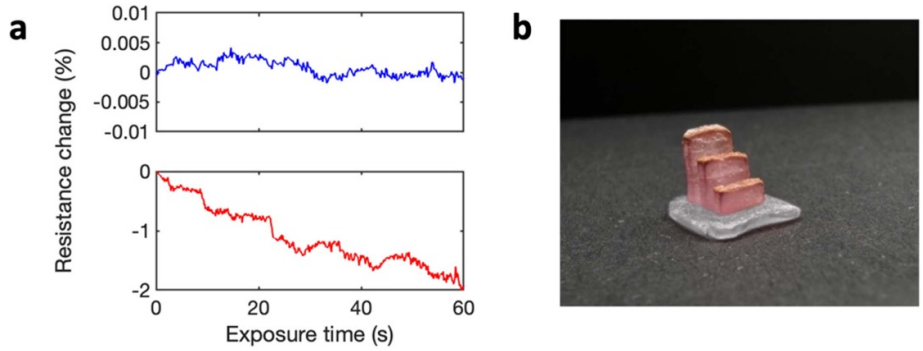

Figure A4. (a) Resistance change of a graphene track printed onto a non-doped glass slab (top) and a AuNP-doped glass slab (bottom) during exposure to continuous illumination with green laser light (550 nm, $P = 25$ mW). (b) Printed glass structures with two different colours. The base is without doping and the standing surfaces are doped with 0.5 mM AuNP.

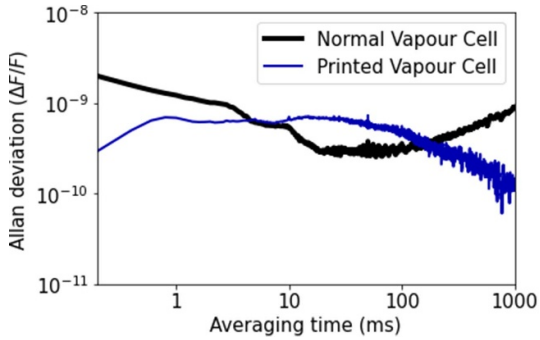

Figure A5. Allan deviation comparison of the printed vapour cell and the commercial vapour cell, adjusted for the ratio of the corresponding optical path lengths.

Appendix E. Polarisation characterization of the printed vapour cell

The stability of the polarization was also measured by analyzing the polarization over time (figure A6). No time-dependent change (e.g. through a local temperature change) in polarization was detected.

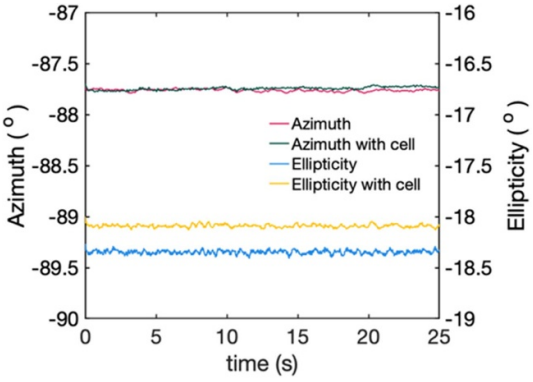

Figure A6. The azimuth and ellipticity measured on a polarisation analyser over time, with and without the presence of the printed vapour cell, for a given incident polarisation.

ORCID iDs

Feiran Wang https://orcid.org/0000-0003-4867-7400
Nathan Cooper https://orcid.org/0000-0001-7866-3267
Yinfeng He https://orcid.org/0000-0003-0325-8675

Ricky D Wildman https://orcid.org/0000-0003-2329-8471
Lyudmila Turyanska https://orcid.org/0000-0002-9552-6501
Lucia Hackermüller https://orcid.org/0000-0001-9880-2914

References

[1] Aslam N, Zhou H, Urbach E K, Turner M J, Walsworth R L, Lukin M D and Park H 2023 Quantum sensors for biomedical applications *Nat. Rev. Phys.* **5** 157–69
[2] Boto E, Holmes N, Leggett J, Roberts G, Shah V, Meyer S S, Muñoz L D, Mullinger K J, Tierney T M and Bestmann S 2018 Moving magnetoencephalography towards real-world applications with a wearable system *Nature* **555** 657–61
[3] Arita Y, Mazilu M and Dholakia K 2013 Laser-induced rotation and cooling of a trapped microgyroscope in vacuum *Nat. Commun.* **4** 2374
[4] Bongs K, Holynski M, Vovrosh J, Bouyer P, Condon G, Rasel E, Schubert C, Schleich W P and Roura A 2019 Taking atom interferometric quantum sensors from the laboratory to real-world applications *Nat. Rev. Phys.* **1** 731–9
[5] Lee J, Lisanti M, Terrano W A and Romalis M 2023 Laboratory constraints on the neutron-spin coupling of fev-scale axions *Phys. Rev.* X **13** 011050
[6] Feng D 2019 Review of quantum navigation *IOP Conf. Ser.: Earth Environ. Sci.* **237** 032027
[7] Stray B, Lamb A, Kaushik A, Vovrosh J, Rodgers A, Winch J, Hayati F, Boddice D, Stabrawa A and Niggebaum A 2022 Quantum sensing for gravity cartography *Nature* **602** 590–4
[8] Evered S J, Bluvstein D, Kalinowski M, Ebadi S, Manovitz T, Zhou H, Li S H, Geim A A, Wang T T and Maskara N 2023 High-fidelity parallel entangling gates on a neutral-atom quantum computer *Nature* **622** 268–72
[9] Vovrosh J, Voulazeris G, Petrov P G, Zou J, Gaber Y, Benn L, Woolger D, Attallah M M, Boyer V and Bongs K 2018 Additive manufacturing of magnetic shielding and ultra-high vacuum flange for cold atom sensors *Sci. Rep.* **8** 2023
[10] Ruchka P, Hammer S, Rockenhäuser M, Albrecht R, Drozella J, Thiele S, Giessen H and Langen T 2022 Microscopic 3D printed optical tweezers for atomic quantum technology *Quantum Sci. Technol.* **7** 045011
[11] Cooper N, Coles L, Everton S, Maskery I, Campion R, Madkhaly S, Morley C, O'Shea J, Evans W and Saint R 2021 Additively manufactured ultra-high vacuum chamber for portable quantum technologies *Addit. Manuf.* **40** 101898
[12] Madkhaly S, Coles L, Morley C, Colquhoun C, Fromhold T, Cooper N and Hackermüller L 2021 Performance-optimized components for quantum technologies via additive manufacturing *PRX Quantum* **2** 030326
[13] Stærkind H, Jensen K, Müller J H, Boer V O, Petersen E T and Polzik E S 2023 Precision measurement of the excited state landé g-factor and diamagnetic shift of the cesium D_2 line *Phys. Rev.* X **13** 021036
[14] Liew L-A, Knappe S, Moreland J, Robinson H, Hollberg L and Kitching J 2004 Microfabricated alkali atom vapor cells *Appl. Phys. Lett.* **84** 2694–6
[15] Maurice V, Carlé C, Keshavarzi S, Chutani R, Queste S, Gauthier-Manuel L, Cote J-M, Vicarini R, Abdel Hafiz M and Boudot R 2022 Wafer-level vapor cells filled with laser-actuated hermetic seals for integrated atomic devices *Microsyst. Nanoeng.* **8** 129
[16] Cooper N, Madkhaly S, Johnson D, Hopton B, Baldolini D and Hackermüller L 2023 Dual-frequency Doppler-free spectroscopy for simultaneous laser stabilization in compact atomic physics experiments *Phys. Rev.* A **108** 013521
[17] Martinez G D, Li C, Staron A, Kitching J, Raman C and McGehee W R 2023 A chip-scale atomic beam clock *Nat. Commun.* **14** 3501
[18] Vilas N B, Hallas C, Anderegg L, Robichaud P, Winnicki A, Mitra D and Doyle J M 2022 Magneto-optical trapping and sub-Doppler cooling of a polyatomic molecule *Nature* **606** 70–74
[19] Häffner H, Roos C F and Blatt R 2008 Quantum computing with trapped ions *Phys. Rep.* **469** 155–203
[20] Marciniak C D, Feldker T, Pogorelov I, Kaubruegger R, Vasilyev D V, van Bijnen R, Schindler P, Zoller P, Blatt R and Monz T 2022 Optimal metrology with programmable quantum sensors *Nature* **603** 604–9
[21] Fabricant A, Novikova I and Bison G 2023 How to build a magnetometer with thermal atomic vapor: a tutorial *New J. Phys.* **25** 025001
[22] Pross A, Crisan A, Bending S, Mosser V and Konczykowski M 2005 Second-generation quantum-well sensors for room-temperature scanning Hall probe microscopy *J. Appl. Phys.* **97** 096105
[23] Behzadirad M, Mecholdt S, Randall J N, Ballard J B, Owen J, Rishinaramangalam A K, Reum A, Gotszalk T, Feezell D F and Rangelow I W 2021 Advanced scanning probe nanolithography using GaN nanowires *Nano Lett.* **21** 5493–9
[24] Pétremand Y, Affolderbach C, Straessle R, Pellaton M, Briand D, Mileti G and de Rooij N F 2012 Microfabricated rubidium vapour cell with a thick glass core for small-scale atomic clock applications *J. Micromech. Microeng.* **22** 025013
[25] Shah V, Knappe S, Schwindt P D and Kitching J 2007 Subpicotesla atomic magnetometry with a microfabricated vapour cell *Nat. Photon.* **1** 649–52
[26] Gong F, Jau Y-Y, Jensen K and Happer W 2006 Electrolytic fabrication of atomic clock cells *Rev. Sci. Instrum.* **77** 076101
[27] Griffith W C, Knappe S and Kitching J 2010 Femtotesla atomic magnetometry in a microfabricated vapor cell *Opt. Express* **18** 27167–72
[28] Lee C-H, Guo H, Radhakrishnam S, Lal A, Szekely C, McClelland T and Pisano A P 2004 A batch fabricated rubidium-vapor resonance cell for chip-scale atomic clocks *Proc. Solid-State Sensors, Actuators and Microsystems Workshop* (*Hilton Head Island, SC, 6–10 June 2004*) pp 23–26
[29] Luo J, Gilbert L J, Qu C, Landers R G, Bristow D A and Kinzel E C 2017 Additive manufacturing of transparent soda-lime glass using a filament-fed process *J. Manuf. Sci. Eng.* **139** 061006
[30] Inamura C, Stern M, Lizardo D, Houk P and Oxman N 2018 Additive manufacturing of transparent glass structures *3D Print. Addit. Manuf.* **5** 269–83
[31] Datsiou K C, Saleh E, Spirrett F, Goodridge R, Ashcroft I and Eustice D 2019 Additive manufacturing of glass with laser powder bed fusion *J. Am. Ceram. Soc.* **102** 4410–4
[32] Lei J, Hong Y, Zhang Q, Peng F and Xiao H 2019 Additive manufacturing of fused silica glass using direct laser melting *CLEO: Applications and Technology* (Optica Publishing Group) pp AW3I–4
[33] Sasan K, Lange A, Yee T D, Dudukovic N, Nguyen D T, Johnson M A, Herrera O D, Yoo J H, Sawvel A M and Ellis M E 2020 Additive manufacturing of optical quality germania–silica glasses *ACS Appl. Mater. Interfaces* **12** 6736–41
[34] Kotz F, Arnold K, Bauer W, Schild D, Keller N, Sachsenheimer K, Nargang T M, Richter C, Helmer D and Rapp B E 2017 Three-dimensional printing of transparent fused silica glass *Nature* **544** 337–9

[35] Cooperstein I, Shukrun E, Press O, Kamyshny A and Magdassi S 2018 Additive manufacturing of transparent silica glass from solutions *ACS Appl. Mater. Interfaces* **10** 18879–85
[36] Moore D G, Barbera L, Masania K and Studart A R 2020 Three-dimensional printing of multicomponent glasses using phase-separating resins *Nat. Mater.* **19** 212–7
[37] Toombs J T, Luitz M, Cook C C, Jenne S, Li C C, Rapp B E, Kotz-Helmer F and Taylor H K 2022 Volumetric additive manufacturing of silica glass with microscale computed axial lithography *Science* **376** 308–12
[38] Kotz F, Quick A S, Risch P, Martin T, Hoose T, Thiel M, Helmer D and Rapp B E 2021 Two-photon polymerization of nanocomposites for the fabrication of transparent fused silica glass microstructures *Adv. Mater.* **33** 2006341
[39] Han D, Yang C, Fang N X and Lee H 2019 Rapid multi-material 3D printing with projection micro-stereolithography using dynamic fluidic control *Addit. Manuf.* **27** 606–15
[40] Barwood G, Gill P and Rowley W 1988 A simple rubidium-stabilised laser diode for interferometric applications *J. Phys. E: Sci. Instrum.* **21** 966
[41] Brookes M J, Leggett J, Rea M, Hill R M, Holmes N, Boto E and Bowtell R 2022 Magnetoencephalography with optically pumped magnetometers (OPM-MEG): the next generation of functional neuroimaging *Trends Neurosci.* **45** 621–34
[42] Cai P, Guo L, Wang H, Li J, Li J, Qiu Y, Zhang Q and Lue Q 2020 Effects of slurry mixing methods and solid loading on 3D printed silica glass parts based on DLP stereolithography *Ceram. Int.* **46** 16833–41
[43] Lucivero V G, Zanoni A, Corrielli G, Osellame R and Mitchell M W 2022 Laser-written vapor cells for chip-scale atomic sensing and spectroscopy *Opt. Express* **30** 27149–63
[44] Yong-Taeg O, Fujino S and Morinag K 2002 Fabrication of transparent silica glass by powder sintering *Sci. Technol. Adv. Mater.* **3** 297–301
[45] Milonjić S K, Čerović L S, Čokeša D M and Zec S 2007 The influence of cationic impurities in silica on its crystallization and point of zero charge *J. Colloid Interface Sci.* **309** 155–9
[46] Kiyose S, Hirai Y, Tabata O and Tsuchiya T 2021 Microfabricated alkali metal vapor cells filled with an on-chip dispensing component *Jpn. J. Appl. Phys.* **60** SCCL01
[47] Palacios Alvarez S, Gomez P, Coop S, Zamora-Zamora R, Mazzinghi C and Mitchell M W 2022 Single-domain Bose condensate magnetometer achieves energy resolution per bandwidth below $\hbar$ *Proc. Natl Acad. Sci.* **119** e2115339119
[48] Liu C, Qian B, Ni R, Liu X and Qiu J 2018 3D printing of multicolor luminescent glass *RSC Adv.* **8** 31564–7
[49] Tabellion J, Zeiner J and Clasen R 2006 Manufacturing of pure and doped silica and multicomponent glasses from SiO_2 nanoparticles by reactive electrophoretic deposition *J. Mater. Sci.* **41** 8173–80
[50] Hu Q, Sun X-Z, Parmenter C D, Fay M W, Smith E F, Rance G A, He Y, Zhang F, Liu Y and Irvine D 2017 Additive manufacture of complex 3D Au-containing nanocomposites by simultaneous two-photon polymerisation and photoreduction *Sci. Rep.* **7** 17150
[51] Sakamoto M, Fujistuka M and Majima T 2009 Light as a construction tool of metal nanoparticles: synthesis and mechanism *J. Photochem. Photobiol.* C **10** 33–56
[52] Le N H, Hajjar-Garreau S, Bonne M, Megías-Sayago C, Louis B, Lebeau B and Balan L 2020 Photo-induced generation of size controlled Au nanoparticles on pure siliceous ordered mesoporous silica for catalytic applications *Microporous Mesoporous Mater.* **295** 109952
[53] Bharadwaj R and Mukherji S 2014 Gold nanoparticle coated U-bend fibre optic probe for localized surface plasmon resonance based detection of explosive vapours *Sens. Actuators* B **192** 804–11
[54] Wang F, Gosling J H, Trindade G F, Rance G A, Makarovsky O, Cottam N D, Kudrynskyi Z, Balanov A G, Greenaway M T and Wildman R D 2021 Inter-flake quantum transport of electrons and holes in inkjet-printed graphene devices *Adv. Funct. Mater.* **31** 2007478
[55] Trindade G F, Wang F, Im J, He Y, Balogh A, Scurr D, Gilmore I, Tiddia M, Saleh E and Pervan D 2021 Residual polymer stabiliser causes anisotropic electrical conductivity during inkjet printing of metal nanoparticles *Commun. Mater.* **2** 47
[56] Austin J S, Cottam N D, Zhang C, Wang F, Gosling J H, Nelson-Dummet O, James T S, Beton P H, Trindade G F and Zhou Y 2023 Photosensitisation of inkjet printed graphene with stable all-inorganic perovskite nanocrystals *Nanoscale* **15** 2134–42
[57] Faria-e-silva A L and Pfeifer C S 2017 Impact of thio-urethane additive and filler type on light-transmission and depth of polymerization of dental composites *Dent. Mater.* **33** 1274–85
[58] Zhao P, He Y, Trindade G F, Baumers M, Irvine D J, Hague R J, Ashcroft I A and Wildman R D 2021 Modelling the influence of UV curing strategies for optimisation of inkjet based 3D printing *Mater. Des.* **208** 109889
[59] Jašo V, Stoiljković D, Radičević R and Bera O 2013 Kinetic modeling of bulk free-radical polymerization of methyl methacrylate *Polym. J.* **45** 631–6